Heavy Alkali Treatment of $Cu(In,Ga)Se_2$ Solar Cells: Surface versus Bulk Effects

Susanne Siebentritt, Enrico Avancini, Marcus Bär, Jakob Bombsch, Emilie Bourgeois, Stephan Buecheler, Romain Carron, Celia Castro, Sebastien Duguay, Roberto Félix, Evelyn Handick, Dimitrios Hariskos, Ville Havu, Philip Jackson, Hannu-Pekka Komsa, Thomas Kunze, Maria Malitckaya, Roberto Menozzi, Milos Nesladek, Nicoleta Nicoara, Martti Puska, Mohit Raghuwanshi, Philippe Pareige, Sascha Sadewasser, Giovanna Sozzi, Ayodhya Nath Tiwari, Shigenori Ueda, Arantxa Vilalta-Clemente, Thomas Paul Weiss, Florian Werner, Regan G. Wilks, Wolfram Witte, and Max Hilaire Wolter*

Chalcopyrite solar cells achieve efficiencies above 23%. The latest improvements are due to post-deposition treatments (PDT) with heavy alkalis. This study provides a comprehensive description of the effect of PDT on the chemical and electronic structure of surface and bulk of $Cu(In,Ga)Se_2$. Chemical changes at the surface appear similar, independent of absorber or alkali. However, the effect on the surface electronic structure differs with absorber or type of treatment, although the improvement of the solar cell efficiency is the same. Thus, changes at the surface cannot be the only effect of the PDT treatment. The main effect of PDT with heavy alkalis concerns bulk recombination. The reduction in bulk recombination goes along with a reduced density of electronic tail states. Improvements in open-circuit voltage appear together with reduced band bending at grain boundaries. Heavy alkalis accumulate at grain boundaries and are not detected in the grains. This behavior is understood by the energetics of the formation of single-phase Cu-alkali compounds. Thus, the efficiency improvement with heavy alkali PDT can be attributed to reduced band bending at grain boundaries, which reduces tail states and nonradiative recombination and is caused by accumulation of heavy alkalis at grain boundaries.

1. Introduction

Thin film solar modules provide electricity with the lowest carbon emissions.[1] Solar cells based on $Cu(In,Ga)Se_2$ thin film absorbers show very high and stable efficiencies for laboratory cells as well as for industrial modules. The recent series of confirmed record efficiencies[2–5] up to 23.4%[6] has been made possible by post-deposition treatments (PDT) based on the heavy alkalis K,[2,3] Rb,[5] or Cs.[5] The treatments have proved to be beneficial on a wide range of $Cu(In,Ga)Se_2$ based absorbers: absorbers containing additionally sulfur[7] or silver,[8] absorbers prepared by co-evaporation by low-temperature[2] or by high-temperature[5] processes, or absorbers prepared by a sequential process,[9] absorbers with low[10] or with high Ga content.[3,11] In all cases the open-circuit voltage (V_{OC}) has been improved as a result of employing heavy alkali PDTs.

Prof. S. Siebentritt, Dr. T. P. Weiss, Dr. F. Werner, Dr. M. H. Wolter
Laboratory for Photovoltaics
Physics and Materials Science Research Unit
University of Luxembourg
41, rue du Brill 4422 Belvaux, Luxembourg
E-mail: susanne.siebentritt@uni.lu

Dr. E. Avancini, Dr. S. Buecheler, Dr. R. Carron, Prof. A. N. Tiwari
Laboratory for Thin Films and Photovoltaics
Empa
Swiss Federal Laboratories for Materials Science and Technology
Überlandstrasse 129
8600 Dübendorf, Switzerland

The ORCID identification number(s) for the author(s) of this article can be found under https://doi.org/10.1002/aenm.201903752.

DOI: 10.1002/aenm.201903752

Prof. M. Bär, J. Bombsch, Dr. R. Félix, Dr. E. Handick, Dr. T. Kunze, Dr. R. G. Wilks
Interface Design
Helmholtz-Zentrum Berlin für Materialien und Energie GmbH (HZB)
12489 Berlin, Germany

Prof. M. Bär, Dr. R. G. Wilks
Energy Materials In-Situ Laboratory Berlin (EMIL)
Helmholtz-Zentrum Berlin für Materialien und Energie GmbH
12489 Berlin, Germany

Prof. M. Bär
Helmholtz-Institute Erlangen-Nürnberg for Renewable Energy (HI ERN)
12489 Berlin, Germany

Prof. M. Bär
Department of Chemistry and Pharmacy
Friedrich-Alexander-Universität Erlangen-Nürnberg
91054 Erlangen, Germany

 © 2020 WILEY-VCH Verlag GmbH & Co. KGaA, Weinheim

These treatments have been scaled for production of full-size industrial modules.[12]

It has long been known that the presence of alkalis, in particular Na, improves the efficiency of Cu(In,Ga)Se_2 solar cells.[13,14] In fact, the presence of Na in the Cu(In,Ga)Se_2 absorber is necessary to achieve reasonable efficiencies.[15,16] The main effect of Na is to improve open-circuit voltage (and thus fill factor), which can be attributed to Na-induced higher net doping levels.[17]

However, the recent improvements go beyond this effect and are only obtained by a post-deposition treatment with heavy alkalis (i.e., higher atomic mass than Na; in this article we use the term "light alkalis" for Li and Na and "heavy alkalis" for K, Rb, and Cs). The first heavy alkali PDT was based on potassium fluoride (KF).[2,18] It became clear early on that this treatment induces changes in the chemistry of the absorber surface.[2,19] This change was found, at least in some cases, to induce a widening of the bandgap at the absorber surface,[19,20] and has been attributed to the formation of a K-In-Se compound (KIS) layer.[21–24] Also, stronger diffusion of Cd from the buffer layer into the KF treated surface was observed.[25] Based on these observations, the improvement in open-circuit voltage has been attributed to a reduced recombination at the absorber-buffer interface,[17,26] although previous record devices without alkali PDT (on a lower performance level) were not limited by interface recombination either.[27] One important effect of the changed surface chemistry is that it is possible to reduce the thickness of the CdS buffer without losses in open-circuit voltage. The thinner buffer layer leads to reduction in its parasitic absorption and thus to an improved short-circuit current.[2,4]

Additionally, from the beginning of experiments with heavy alkali treatment there have been indications that the treatment changes not only surface but also bulk properties of the absorbers. When comparing the heavy alkali treated absorbers to those that already contain Na, either due to diffusion from the glass substrate or due to a sodium fluoride (NaF)-PDT, a change in doping density is observed. In most cases a slight increase in the net doping density is reported.[7,28,29] However, particularly for absorbers prepared by a low-temperature process, a decrease in net doping density has also been observed.[17] Furthermore, an increase in the minority carrier lifetime, i.e., reduction of nonradiative recombination, was observed.[28] In general, it is observed that alkali elements segregate at grain boundaries.[30,31] Already in the very first studies on heavy alkali PDT it was shown that the heavy alkali partly replaces the sodium that is present without the heavy alkali PDT.[2,21] It was, therefore, proposed that grain boundary passivation is important for the observed changes.[32]

In this contribution we compare the effect of heavy alkali treatment on Cu(In,Ga)Se_2 absorbers prepared by co-evaporation at high and at low substrate temperatures. The high-temperature absorbers are prepared on Na-containing glass substrates. Therefore, Na, as well as some K, diffuses during the Cu(In,Ga)Se_2 deposition process at elevated temperatures into the absorber. Thus, Na (and some K) is present in the absorber without the need for PDT. These absorbers received a PDT with heavy alkalis only (i.e., with either potassium fluoride (KF), rubidium fluoride (RbF), or cesium fluoride (CsF)). Afterward a buffer layer, typically solution grown CdS, is deposited onto the absorber. Our best solar cell efficiency using high-temperature absorbers with KF treatment is 20.8%,[3] with RbF treatment 22.6%,[5] and with CsF 21.6% (**Figure 1**). A low-temperature process has been

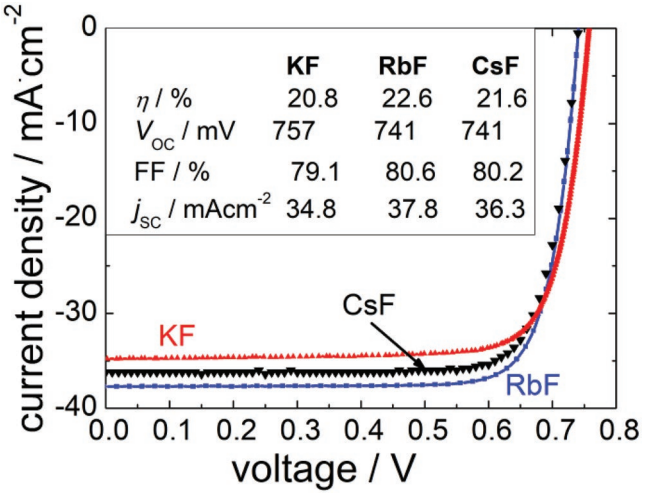

Figure 1. IV measurements of the best-performing solar cells after heavy alkali PDT, based on a high-temperature Cu(In,Ga)Se_2 absorber. The area of the cells is 0.5 cm^2. The cells have an antireflective coating. Note: the KF[3] and RbF[5] treated cells are presented by certified measurements performed at Fraunhofer ISE; the IV of the CsF treated cell is measured in house at ZSW.

Dr. E. Bourgeois, Prof. M. Nesladek
IMO-IMOMEC
Universiteit Hasselt – Campus Diepenbeek
Wetenschapspark 1, B-3590 Diepenbeek, Belgium

Dr. C. Castro, Prof. S. Duguay, Dr. M. Raghuwanshi, Prof. P. Pareige, Dr. A. Vilalta-Clemente
Groupe de Physique des Matériaux (GPM)
Normandie Université
UNIROUEN
Insa Rouen UMR 6634, 76000 Rouen, France

Dr. D. Hariskos, P. Jackson, Dr. W. Witte
Zentrum für Sonnenenergie- und Wasserstoff-Forschung
Baden-Württemberg (ZSW)
Meitnerstraße 1, 70563 Stuttgart, Germany

Dr. V. Havu, Dr. H.-P. Komsa, Dr. M. Malitckaya, Prof. M. Puska
Department of Applied Physics
Aalto University
P.O. Box 11000, 00076 Aalto, Finland

Prof. R. Menozzi, Prof. G. Sozzi
Department of Engineering and Architecture
University of Parma
Parco Area delle Scienze 181A, 43124 Parma, Italy

Dr. N. Nicoara, Dr. S. Sadewasser
INL – International Iberian Nanotechnology Laboratory
Av. Mestre José Veiga s/n
4715-330 Braga, Portugal

Dr. S. Ueda
NIMS Beamline Station at SPring-8
National Institute for Materials Science (NIMS), Kouto
Sayo, Hyogo 679-5198, Japan

Dr. A. Vilalta-Clemente
Institut Pprime, CNRS, ENSMA, Université de Poitiers
UPR CNRS 3346
Physics and Mechanics of Materials Department
ENSMA
Téléport 2, 1 avenue Clément Ader, BP 40109, 86961
Futuroscope Chasseneuil Cedex, France

© 2020 WILEY-VCH Verlag GmbH & Co. KGaA, Weinheim

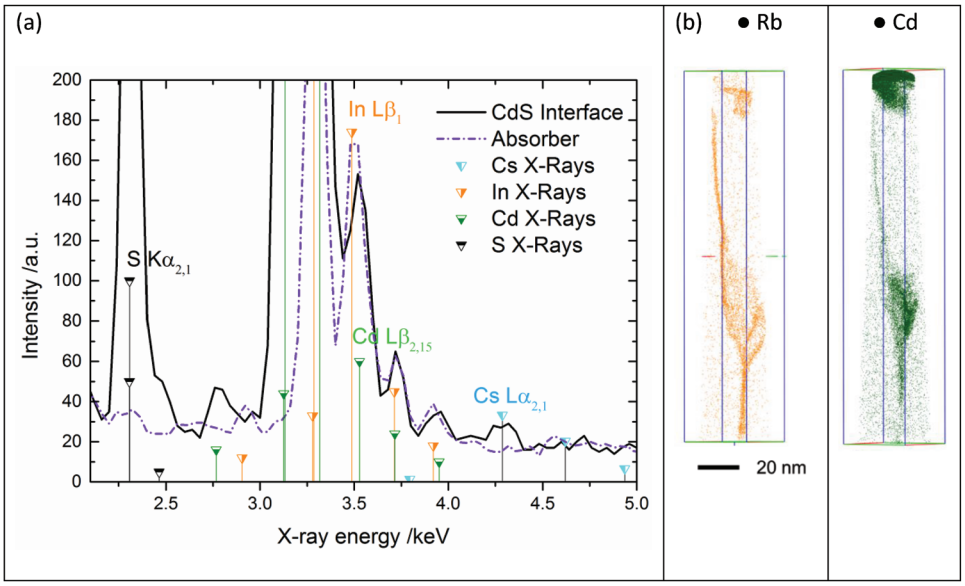

Figure 2. a) EDS spectra extracted from a STEM-EDS profile at the Cu(In,Ga)Se_2/CdS interface (black line) and inside the absorber (purple dash-dot line) from a CsF-treated high-temperature absorber. The absorber matrix element In is detected in both spectra, whereas the buffer matrix elements Cd and S and in addition Cs are only detected at the Cu(In,Ga)Se_2/CdS interface. b) 3D reconstructions of an APT analysis of an RbF-treated high-temperature absorber, $^{85}Rb^+$ and $^{112}Cd^+$ isotopes are shown. Rb and Cd accumulate at grain boundaries inside the Cu(In,Ga)Se_2 absorber and at the Cu(In,Ga)Se_2/CdS interface. Note that the APT tip has been prepared with the tip axis parallel to the CdS/CIGS interface. The analysis is, thus, at or within a few ten nanometers below the interface. The high concentration of Cd atoms indicates the location of the Cu(In,Ga)Se_2/CdS interface; the increased concentration, appearing as a thin line in the projection, indicates a grain boundary.

developed for flexible (and temperature sensitive) substrates,[33] which, unlike glass substrates, contain no alkali atoms. In the study presented here, either substrates of glass with a SiO_x diffusion barrier (to prevent alkali diffusion into the absorber) or alkali-free flexible substrates are used for the low-temperature absorbers. Thus, no Na diffuses from the substrates, and so these absorbers are subjected to a double PDT: first with NaF, and then with either KF or RbF. The best efficiency for low-temperature absorbers is 20.4% with NaF+KF treatment[2] and 20.8% with NaF+RbF treatment[34]—both achieved on flexible substrates.

In the following, we first discuss the effects of PDT with heavy alkalis on the surface and on the bulk of the Cu(In,Ga)Se_2 absorbers, and then discuss differences between treatments with heavy and with light alkalis.

2. Effects of Post-Deposition Treatment with Heavy Alkalis

The effects of PDT with fluorides of the heavy alkali elements, i.e., KF, RbF, or CsF, on the chemical and optoelectronic properties of the surface and the bulk of Cu(In,Ga)Se_2 absorbers prepared by different processes have been investigated and analyzed in view of their potential contribution to the observed improvement of the open-circuit voltage.

2.1. Surface Effects

The first clearly observed effect of KF-PDT was a change in surface chemistry with potassium accumulating at the surface, leading to a change of Cu(In,Ga)Se_2 surface composition.[2,18] The observed effects in KF-treated materials motivated us to study whether or not Rb or Cs treatments produce a similar surface modification.

Scanning transmission electron microscopy–energy dispersive X-ray spectroscopy (STEM-EDS) and atom probe tomography (APT) are powerful techniques to study the distribution of elements at nanometer scale. Cu(In,Ga)Se_2 solar cells grown at high temperature with either RbF-PDT or CsF-PDT were analyzed using both of these high resolution techniques. In **Figure 2**a, we compare STEM-EDS spectra of a CsF-treated absorber taken at the Cu(In,Ga)Se_2/CdS interface with those taken inside the Cu(In,Ga)Se_2 layer. The Cs Lα_1 X-ray emission line at 4.286 keV is clearly detected at the Cu(In,Ga)Se_2/CdS interface but not inside the absorber. Similar observations for RbF-treated Cu(In,Ga)Se_2 are presented by Vilalta-Clemente et al. and Raghuwanshi et al.[35,36]

The Cu(In,Ga)Se_2/CdS interface of the RbF-treated sample was successfully analyzed by APT although the evaporation field variation and the mechanical stress exerted by taking an APT measurement across an interface render these analyses very difficult. Volume reconstructions in Figure 2b of $^{85}Rb^+$ and of $^{112}Cd^+$ isotopes demonstrate the Rb accumulation at the Cu(InGa)Se_2/CdS interface and at the grain boundaries (the latter is also true for Cd). Within the grain, Cd and Rb concentrations are below the detection limit of APT (10 ppm in the present set of data). For CsF-treated samples the overlap in the mass spectra between $^{115}In^+$+H_2O molecular ions and $^{133}Cs^+$ ions prevents the determination of the Cs distribution within the Cu(In,Ga)Se_2 absorber by APT.

© 2020 WILEY-VCH Verlag GmbH & Co. KGaA, Weinheim

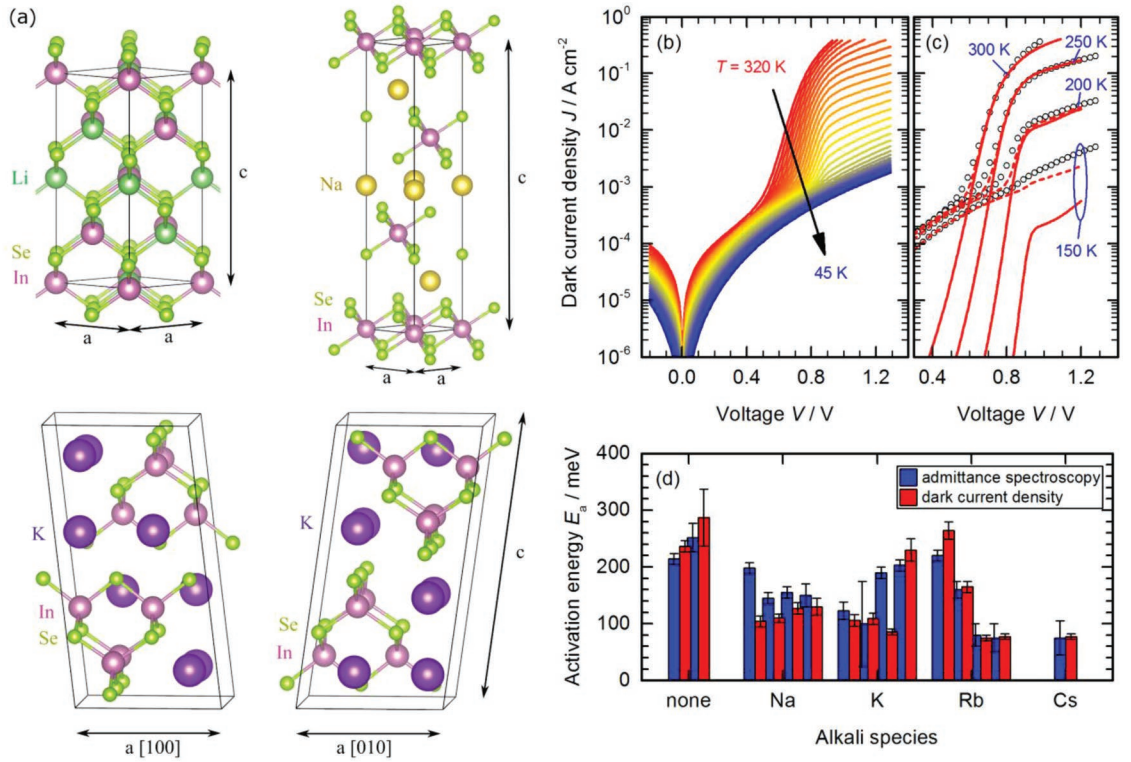

Figure 3. a) Structures of $AlkInSe_2$ (Alk = Li, Na, K, Rb, Cs) compounds, calculated by DFT. Li and Na compounds crystallize as a tetragonal chalcopyrite and a trigonal delafossite structure, respectively, whereas K, Rb, and Cs compounds prefer a layered monoclinic structure shown in two perpendicular views for $KInSe_2$. The calculated bandgap of $KInSe_2$ (2.53 eV)[42] agrees well with the surface bandgap of 2.5 eV, experimentally observed on KF- treated $Cu(In,Ga)Se_2$.[20] b,c) Experimental and simulated IVT curves in the dark at lower temperature (dashed lines include a nonlinear shunt current to best match the experimental IV curves below 0.5 V) indicate a barrier that is best described by a front side barrier.[46] d) The barrier heights, extracted from admittance spectroscopy and from IV measurements, are independent of the alkali treatment,[46] with possibly a slightly lower barrier for the heavy alkalis Rb and Cs. The $Cu(In,Ga)Se_2$ front side barrier is much more likely due to a cliff at the buffer-window interface than due to an Alk-In-Se layer with a wider bandgap between the absorber and the buffer.

The presented measurements indicate that RbF and CsF-PDT result in an accumulation of the alkali element at the surface of the absorber, in a similar manner as after KF-PDT.[2,37] It should be noted that differences in the exact surface chemistry of KF and of RbF treated absorbers have been observed.[38] The accumulation of potassium near the surface has been interpreted as the formation of a K-In(Ga)-Se compound, sometimes labeled the "KIS layer."[21,37] The formation of a novel compound is supported by the observation that the surface bandgap of KF-treated low-temperature absorbers is considerably higher than that of untreated ones.[20]

The observed accumulation of Rb and Cs at the surface of treated absorbers could indicate that a similar compound is formed at the surfaces of absorbers treated with RbF and CsF. In fact, a very thin $RbInSe_2$ layer was observed by transmission electron microscope (TEM) at the $Cu(In,Ga)Se_2$/CdS interface in RbF-treated samples, while this compound seems to be absent at the In-free $CuGaSe_2$/CdS interface.[39] However, very little information about the chemical and physical properties of these alkali indium selenide compounds is available.[22,40,41] Therefore, we calculated the most stable structures of these compounds by density functional theory (DFT) employing a hybrid functional[42] (**Figure 3**a). For $LiInSe_2$ and $NaInSe_2$, our calculations predict a tetragonal chalcopyrite and a delafossite structure with bandgaps of 2.60 and 2.16 eV, respectively. All heavy alkali compounds, $KInSe_2$, $RbInSe_2$, and $CsInSe_2$ are found to crystallize in a layered monoclinic structure with bandgaps of 2.53, 2.57, and 2.66 eV, respectively. The calculated bandgap of $KInSe_2$, 2.53 eV, is in excellent agreement with the surface bandgap found experimentally at KF-treated $Cu(In,Ga)Se_2$ absorbers.[20] From photoemission spectroscopy (PES) and inverse photoemission spectroscopy (IPES), it was concluded that part of this bandgap widening is due to an upward shift of the conduction band by 0.4 eV.[20] A continuous layer with the conduction band edge so high in energy would be expected to form a barrier for electron transport, which should be visible in temperature dependent current–voltage (IVT) characteristics and in admittance spectroscopy. In fact, on an RbF-treated low-temperature absorber, a reduction of the measured barrier was observed after etching the treated film and supposedly reducing the thickness of a Rb-In-Se layer, see Figure S1 in the Supporting Information and ref. [43]. However, our DFT modeling of band offsets for idealized model interfaces between $CuInSe_2$ and $KInSe_2$, $RbInSe_2$, and $CsInSe_2$ shows actually downward shifts of the conduction band edge,[44] see Figure S2 in the Supporting Information. The recent DFT modeling by Ghorbani et al.[45] predicts that Cu deficiency shifts the conduction band of $CuInSe_2$ downward but this cannot totally cancel

© 2020 WILEY-VCH Verlag GmbH & Co. KGaA, Weinheim

the computed downward shift of the conduction band from $CuInSe_2$ to alkali secondary phases (Figure S2, Supporting Information), even in the case of the smallest shift for $KInSe_2$. Resolution for this discrepancy between experimental and theoretical findings remains a topic of future research.

In Figure 3b we show experimental temperature-dependent IV characteristics of a treated high-temperature absorber, measured in the dark, which indicates a transport barrier in the device, as well: The dark current in forward bias decreases drastically when the device is cooled down, and current flow across the device below 130 K (for the device shown in Figure 3b) occurs purely by shunt currents bypassing the p/n junction of the solar cell. Numerical device simulations shown in Figure 3c confirm that conduction band offsets at the front of the device explain the experimental IVT behavior well.[46,47] These findings, however, cannot be taken as evidence for an alkali-induced interface barrier: We find that the typical shape of experimental IVT characteristics is mostly defined by thermionic emission over a "cliff-like" injection barrier for electrons inside the buffer/window stack. A large conduction band spike between absorber and buffer—or alternatively between absorber and alkali-related surface layer—would instead act as extraction barrier for photo-excited electrons and would thus mostly reduce the fill factor of the solar cell,[47] which we do not observe experimentally. A detailed comparison between simulated and experimental IVT characteristics under illumination can be found in Figure S3 in the Supporting Information.

Admittance spectroscopy confirms the presence of a transport barrier in all investigated devices.[46] We find a clear correlation between the activation energies obtained from the dominant capacitance step in admittance spectroscopy (at zero dc bias voltage, blue bars in Figure 3d) and obtained from the temperature-dependent dark current density (at 0.9 V forward bias, red bars in Figure 3d). These activation energies, determined on a range of different solar cell devices, vary between ≈60 and 300 meV, and show no clear trend with alkali treatment. If there is any trend at all, it is that the barrier is most pronounced without any alkalis present (absorber deposited at low temperatures with Na diffusion barrier, no alkali PDT), and is lower with heavy alkalis. Nevertheless, the spread in activation energies can be considerable for the same alkali species, even for nominally identical devices. Combining all evidence from electrical dc and ac measurements, the transport barrier at the front side of the device is most likely related to conduction band offsets within the CdS/ZnO buffer/window stack, and not to a potential alkali-In-Se surface layer with a wider bandgap, albeit the barrier is influenced by the treatment (Figure S1, Supporting Information). Such a layer with a wider bandgap might still exist at the front interface; but it is not necessarily continuous. In particular, it does not appear to affect the electrical transport characteristics of the solar cell in any significant way.

The formation of a new compound should also affect the binding energies of the concerned elements. In fact, additional species of In and Se have been observed by PES on the surface of KF treated low-temperature absorbers.[24] In a similar study on high-temperature absorbers, however, we do not find any indication of an additional Se species (Figure S4, Supporting Information). To study how the alkali PDT impacts the near-surface region of $Cu(In,Ga)Se_2$ absorbers, we have used photoemission spectroscopy employing hard X-rays, soft X-rays, and ultraviolet (UV) light, changing the photoelectrons' inelastic mean free paths (IMFP) from 12 to below 1 nm[48] and altering the exponential information depth accordingly. **Figure 4** shows a summary of our previously published data[20,24,49] on low-temperature $Cu(In,Ga)Se_2$ samples together with new data on low- and on high-temperature absorbers with KF-PDT. The spectra and fits are shown in Figure S4 in the Supporting Information. The valence band maximum position (VBM, relative to the Fermi level E_F, derived by linear approximation of the leading edge) is presented as a function of the K:Se ratio (determined using Se 3d and K 3s core level lines). The VBM positions and K:Se ratios were measured using different photon energies, and so the exponential distribution of

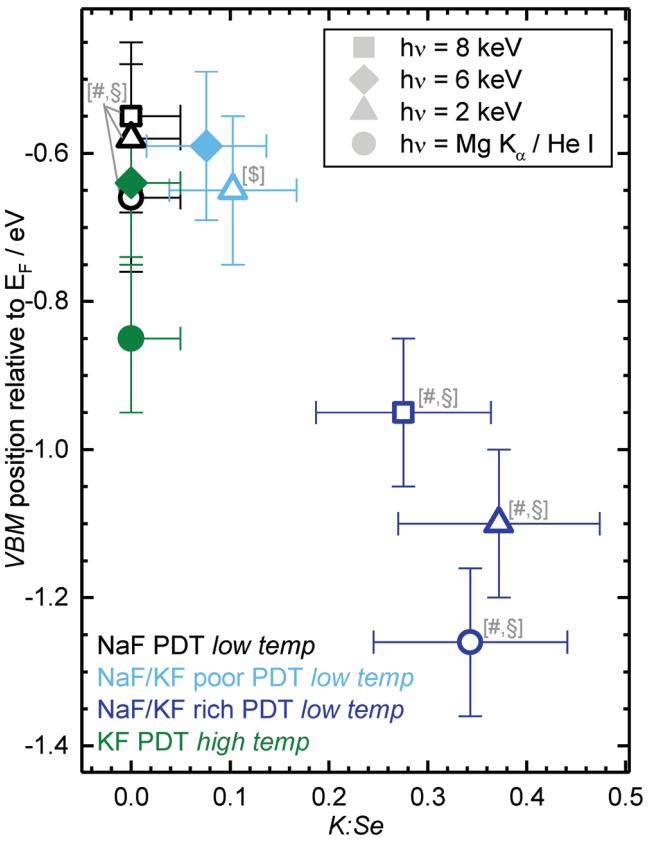

Figure 4. Position of the VBM with respect to the Fermi level E_F and the K:Se ratio of differently treated $Cu(In,Ga)Se_2$ samples derived from photoelectron spectroscopy measurements performed using various excitation energies combined. The different excitation energies relate to inelastic mean free paths (IMFP) of ≈12 nm (8 keV), 10 nm (6 keV), 4 nm (2 keV), 3 nm (Mg K_α), and <1 nm (He I). For the most surface sensitive measurements (lowest excitation energies), VBM values measured with He I are combined with K:Se measurements obtained from Mg K_α measurements, i.e., information with a certain IMFP spread is combined (see ref. [50] for more details). The open symbols represent data previously published:#,[20] §,[24] $;[49] the solid symbols represent new and unpublished data. The respective spectra of the latter can be found in Figure S4 in the Supporting Information. We compare absorbers grown by the high-temperature process (green) with low-temperature absorbers (blue). The latter have been treated using a high ("rich") or low ("poor") deposition rate of the KF.

© 2020 WILEY-VCH Verlag GmbH & Co. KGaA, Weinheim

the signal (the IMFP) varies accordingly; the depth-dependent information is included in the figure. For all PDT samples, whether deposited at low or high temperatures, the VBM measured with more surface sensitive methods is shifted away from the Fermi level relative to the less surface-sensitive measurements. For the NaF+KF treated low-temperature absorbers the shift increases with increasing KF evaporation rate ("NaF/KF rich PDT"). When comparing the VBMs and K:Se ratios of the two differently NaF+KF treated low-temperature samples (poor [rate 1–1.5 nm min^{-1}] and rich [1.5–2 nm min^{-1}]) at different depths it can be observed that the shift in VBM is roughly proportional[50] to the K:Se ratio. For these samples, the VBM shift was related to a surface bandgap widening due to the formation of a Cu- and Ga-free K-In-Se compound at the absorber surface;[20,24] the thickness of this layer varies with KF evaporation rate during PDT (i.e., poor and rich).[49] For the high-temperature samples, however, a similar change in VBM relates to a much lower K:Se ratio. In fact, the K 3s peak, which was used to calculate this ratio, is below the detection limit for the high-temperature $Cu(In,Ga)Se_2$ absorbers. However, the K 2p peak, which has a photoionization cross-section one order of magnitude larger,[51] indicates at least a small amount of K is present near the sample surface. Therefore, it appears that less K is necessary to cause a given shift in VBM on high-temperature absorbers than on low-temperature ones. Comparing poor and rich KF-PDT reveals that the rich treatment leads to a considerably higher concentration of K on the absorber surface and a much more pronounced downward shift of the valence band. On the other hand, the high-temperature absorbers show hardly any potassium at the surface, but the downward shift of the valence band falls between those of the poor and rich KF-PDT low-temperature absorbers, which might suggest a somewhat different PDT mechanism in the high-temperature case.

It thus appears that the chemistry and electronic structure at the surface of these KF-treated absorbers is quite different, although all of them, when completed to solar cells, show very similar improvements in the open-circuit voltage compared to those without heavy alkali treatment. Similar differences occur when comparing the surface bandgap of low-temperature absorbers treated with KF, where a widening of the bandgap was observed,[20] to high-temperature absorbers treated with RbF, where no surface bandgap widening was observed.[52] Furthermore, the additional surface layer on KF- or RbF-treated low-temperature absorbers can in many cases be observed directly by scanning electron microscopy (SEM) as an additional structured layer on the surface.[37,53] Similar structures have been observed on KF-treated $CuInSe_2$ absorbers, prepared by a high-temperature process,[54] however, such structures are not observed on high-efficiency high-temperature $Cu(In,Ga)Se_2$ absorbers after RbF or CsF treatment. Examples of SEM micrographs of the surface of untreated and treated high-temperature absorbers can be found in Figure S5 in the Supporting Information, and no structuring is detectable on these surfaces. Thus, after the alkali-fluoride PDT the surface bandgap can be wider than at the untreated surface or not. In some cases a separate alkali-In-Se layer is clearly observed, in other cases it is not observed. Still, the absorbers with all these different surfaces lead to the same improvement in open-circuit voltage of solar cells. Thus, the surface modification does not appear to be the main driver of the efficiency improvement. Clearly, there are changes to the composition and the electronic structure of the treated absorber surface. These changes can improve the efficiency in various ways, but they appear not to be the main effect that improves the open-circuit voltage.

In summary, our results confirm that the surface of $Cu(In,Ga)Se_2$ is modified after PDT with Rb or Cs, as was already known for KF treatments. However, this surface modification is different for different absorbers and the chemical and electronic properties differ on differently grown and treated absorbers (high- vs low-temperature and poor vs rich alkali treatment), although all of them show a similar improvement of the open-circuit voltage with the alkali PDT. These observed differences together with the lack of correlation of a transport barrier with the alkali treatment indicate that absorber surface modifications are not likely the main driver for higher open-circuit voltages.

2.2. Bulk Effects

In light of the above findings, the following section describes investigations of the effects of the alkali PDT on the $Cu(In,Ga)Se_2$ bulk.

From the observed improvement in V_{OC} it is obvious that the PDT reduces nonradiative recombination. So far, it has been suggested that the PDT reduces nonradiative recombination at the interface.[17,26] Photoluminescence is used to investigate the radiative recombination. Intensity calibrated photoluminescence allows to quantify the ratio of radiative to total recombination, measured as the external radiative efficiency (ERE) which is simply the ratio of the number of photons-out over the number of photons-in. The photons unaccounted for in this ratio must consequently be lost by nonradiative recombination. Thus, photoluminescence measurements give information on the nonradiative recombination. **Figure 5**a compares the radiative efficiency in $Cu(In,Ga)Se_2$ absorbers with and without alkali treatment. We consider bare high-temperature and low-temperature absorbers, as well as absorbers covered with a solution-grown CdS layer (same as the buffer used in solar cells). The bare absorbers show lower radiative efficiency, because they were exposed to air and degraded.[55] Independent of whether the surface is covered with CdS or not, all samples show the same trend: an increase in the radiative efficiency (i.e., a decrease in nonradiative recombination) with the (heavy) alkali treatment. A Na treatment of low-temperature absorbers already increases radiative efficiency, i.e., reduces nonradiative recombination. This effect is attributed to the increase in net doping with Na,[17] as discussed in the introduction. A further decrease in nonradiative recombination is observed with the combined NaF+RbF treatment on low-temperature absorbers, which is in line with the improved open-circuit voltage. The high-temperature absorbers already contain Na from the substrate. Upon adding the heavy alkali by post-deposition treatment the nonradiative recombination in high-temperature absorbers is reduced as well. The reduction in nonradiative recombination is also described by an increase of the quasi-Fermi level splitting. We have demonstrated previously that the quasi-Fermi level

© 2020 WILEY-VCH Verlag GmbH & Co. KGaA, Weinheim

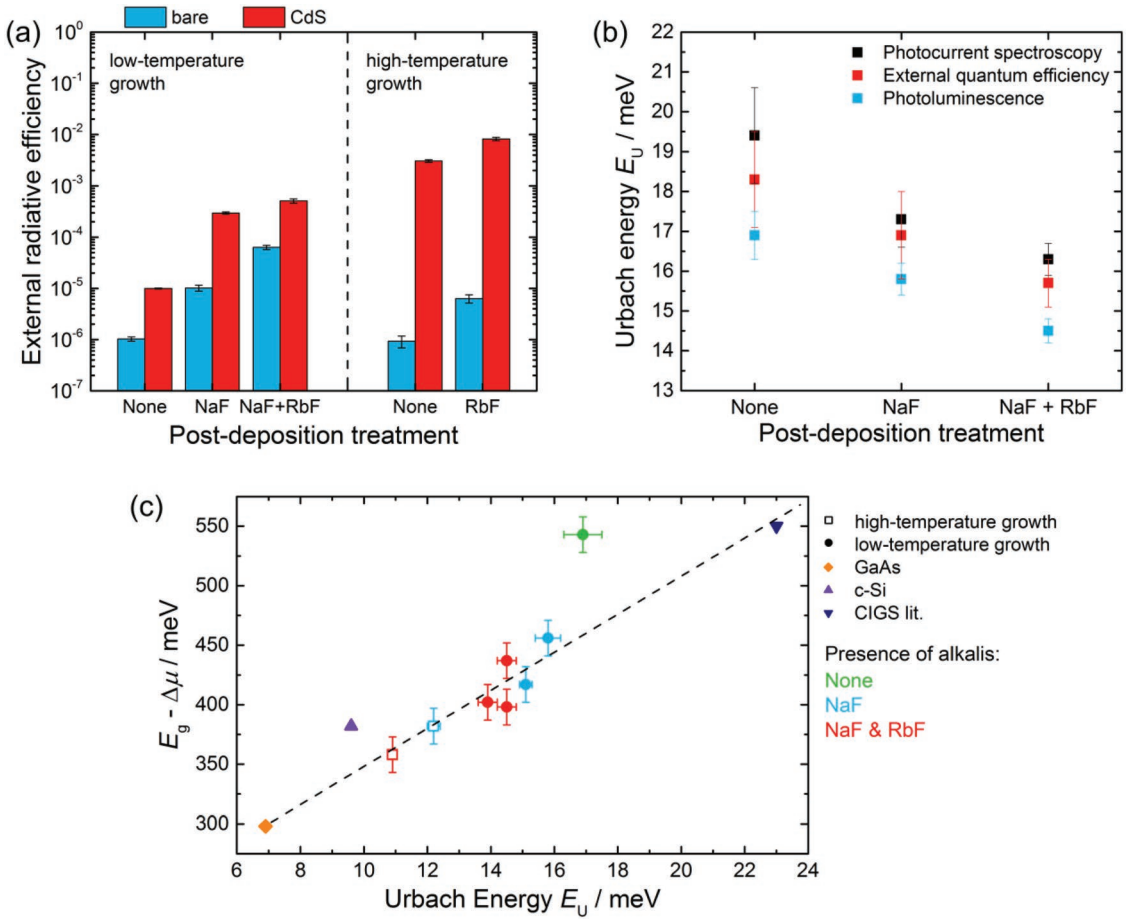

Figure 5. a) Radiative efficiency of absorbers with and without alkali treatment. The radiative efficiency increases with alkali treatment, more so with heavy alkali treatment. This means that the nonradiative recombination is decreased. The improvement is even visible on air-exposed, i.e., degraded absorbers without CdS coverage ("bare"). Note, that the high-temperature absorbers without PDT ("none") contain Na and some K from the glass substrate. b) Urbach energy of low-temperature $Cu(In,Ga)Se_2$ absorbers, measured by various methods, of absorbers with and without alkali treatments, indicating a reduction of the band tailing with PDT, with the strongest reduction for RbF-PDT. Both trends are also observed for high-temperature $Cu(In,Ga)Se_2$ absorbers (see panel (c) and Figure S6 in the Supporting Information). Both observations indicate that the bulk of the absorber is improved. c) Relationship between open-circuit voltage and Urbach energy, together with literature data (for references see text) indicating that the improvement in V_{OC} can be explained by the reduction of band tailing.

splitting increases with RbF-PDT on low-temperature absorbers by about the same amount as the open-circuit voltage.[56] A similar increase in quasi-Fermi level splitting, in parallel to the V_{OC} increase, is observed upon RbF-PDT on high-temperature absorbers (Figure S6, Supporting Information). If recombination at the surface/interface is a major contribution to nonradiative recombination, then the effect of this nonradiative recombination will be more visible in the open-circuit voltage than in the quasi-Fermi level splitting. The surface recombination will reduce the quasi-Fermi level splitting at the surface. But quasi-Fermi level splitting will increase within a diffusion length toward the bulk. Because the higher quasi-Fermi level splitting leads also to higher luminescence intensity[57] the photoluminescence measurement will detect the higher quasi-Fermi level splitting in the bulk, whereas V_{OC} is limited by the smaller quasi-Fermi level splitting at the surface.[58] However, this difference is minimized in absorbers with good transport properties, i.e., long diffusion length, typical for these high efficiency absorbers. The fact that quasi-Fermi level splitting and open-circuit voltage increase by the same amount upon treatment could hint that the reduction of nonradiative recombination occurs mostly in the bulk of the absorber, not at the surface. Furthermore, we observe that the logarithm of the radiative efficiency or the quasi-Fermi level splitting (Figure 5a, Figure S6, Supporting Information, and ref. [56]) increase by similar amounts upon the PDTs in bare and in CdS covered absorbers, which have a very different interface. This similarity is another hint, that the reduction in bulk recombination is more important than the reduction in interface recombination. We thus propose that the main effect of the PDT is to reduce nonradiative recombination in the bulk of the absorber. This conclusion prompts the question: what actually changes in the bulk of the absorbers to create the observed reduction in nonradiative recombination? A possible reason could be the reduction of deep defects. However, we have demonstrated in the past[46] that in state-of-the-art $Cu(In,Ga)Se_2$ absorbers, which result in solar cell efficiencies above 20% and which are investigated in the present study, no deep defects are observable even

© 2020 WILEY-VCH Verlag GmbH & Co. KGaA, Weinheim

without heavy alkali treatment. Recently it has been argued that band tail states are responsible for the deficit in open-circuit voltage.[59,60] Therefore, we investigate the tail states in treated and untreated absorbers by different methods (Figure 5b). We find that the tails can be described by an exponential energy dependence of the density of states with an Urbach energy as the characteristic energy.[61] Although the methods based on transport measurements (black and red dots in Figure 5b) show a somewhat higher Urbach energy than the one determined from photoluminescence measurements, they all show the same trend: a reduction of the Urbach energy, i.e., suppression of tail states, due to alkali treatments. The difference between the Urbach energy values determined by different methods can at least be partly explained by the fact, that photoluminescence can measure lower absorption values and thus measures the Urbach energy deeper in the gap than do transport based techniques.[62] It becomes obvious, in all cases, that the alkali treatments decrease the amount of tail states. This is clearly a bulk effect and not an effect of the absorber surface. The tail states are already reduced after a NaF treatment and are further reduced by the combined NaF+RbF treatment. The same trend is observed in low-temperature and high-temperature absorbers (see Figure 5c). In Figure 5c we summarize the relationship between open-circuit voltage loss (with respect to the bandgap) and Urbach energy for a number of treated and untreated high-temperature and low-temperature absorbers, together with literature data for Cu(In,Ga)Se_2,[59] GaAs,[63,64] and Si.[64,65] For the bandgaps of the Cu(In,Ga)Se_2 samples, we used the bandgap energy, derived for the notch of the Ga concentration profile, as determined by secondary ion mass spectroscopy depth profiling, following the composition-bandgap relationship derived in ref. [66]. We find the same linear relationship between open-circuit voltage loss and Urbach energy as in ref. [59]. Only two data points (crystalline Si and one Cu(In,Ga)Se_2 film) deviate from the linear relationship, displaying a higher open-circuit voltage loss than predicted by the Urbach energy, indicating that in these two cases losses other than those due to tail states, dominate. The reason why Si deviates from the linear relationship could be due to the indirect bandgap of Si and the dominance of Auger recombination in that material. The Cu(In,Ga)Se_2 sample that deviates from the linear relationship is based on the alkali-free absorber and is likely dominated by recombination paths other than recombination through tail states. The generally observed linear relationship indicates that in state-of-the-art Cu(In,Ga)Se_2 solar cells the open-circuit voltage is limited by nonradiative recombination through tail states. The comparison between differently treated absorbers shows that tail states are reduced by the alkali treatments.

Tail states can be caused by any imperfection of the crystal. In polycrystalline Cu(In,Ga)Se_2 absorbers they can be caused by electrostatic potential fluctuations,[67] by bond length variations,[68] by composition variations that change the bandgap,[69] and by effects of grain boundaries.[70] To study the effect of different alkali-fluoride PDTs on the electrostatic band bending at grain boundaries, Kelvin probe force microscopy (KPFM) experiments were performed on a set of three samples where the Cu(In,Ga)Se_2 absorber was grown by an identical high-temperature process (which was optimized for RbF-PDT) and subsequently a KF-, RbF-, or CsF-PDT was applied.[71] From KPFM topography and contact potential difference (CPD) images (**Figure 6**), the potential profile across the grain boundaries was extracted[72] for a total of nearly 240 grain boundaries. For each profile the potential variation at the grain boundary was analyzed (Figure 6c) and all data were statistically evaluated (Figure 6d). We note that the potential variation is likely related to band bending at the grain boundary.[73] For all three alkali-treated samples a fraction of the grain boundaries shows no potential variation ($\Delta CPD_{GB} = 0$), as indicated by the percentage numbers in the figure. Also, all samples show grain boundaries with positive potential variation, corresponding to a barrier for minority charge carriers (electrons), whereas only the sample with KF-PDT shows also grain boundaries with negative potential variation ($\Delta CPD_{GB} < 0$), corresponding to a transport barrier for majority carriers (holes). We propose that this downward band bending leads to losses in the device performance, specifically via a loss in open-circuit voltage. The corresponding V_{OC} values of reference devices prepared with a solution-grown Zn(O,S) buffer layer on the same treated absorber layers are also given in the figure, showing a lower V_{OC} for the KF-treated absorber by 180 mV with respect to the RbF-treated absorber, for which the Cu(In,Ga)Se_2 growth and PDT process were optimized. Remarkably, the potential variations observed for the sample with RbF-PDT are smaller and show significantly less variation compared with those for the KF- and CsF-treated samples. The corresponding solar cells also show the highest open-circuit voltage. In fact, for KF-treated Cu(In,Ga)Se_2, a reduced variation of band bending at grain boundaries was previously also observed,[74] and it was shown by numerical simulations that smaller downward band bending at grain boundaries leads to higher open-circuit voltage.[75] This observation indicates that successful alkali PDTs which lead to an improved open-circuit voltage also reduce the band bending (or at least its variation) at grain boundaries.[71] This observation confirms several numerical studies that show that increased band bending at grain boundaries reduces solar cell efficiency, particularly by reducing the open-circuit voltage.[71,75,76]

If the heavy alkali PDT reduces the band bending at grain boundaries, it means that the number of charged defects in the grain boundaries has been reduced. Thus, chemical changes at the grain boundaries are expected. Accumulation of sodium and potassium at grain boundaries has been observed in the past.[31] Here, we investigate the compositional changes at the grain boundaries, with and without PDT. An accumulation of Rb at the grain boundaries is in fact observed by APT (**Figure 7**). APT analysis of an untreated (Figure 7a,b) and a RbF treated high-temperature Cu(In,Ga)Se_2 absorber (Figure 7c,d) are compared. Figure 7a,c are APT volume reconstructions containing a grain boundary. Elemental profiles extracted from these volumes are presented in Figure 7b,d. In both cases, alkali elements (detected as $^{23}Na^+$, $^{39}K^+$, or $^{85/87}Rb^+$) clearly segregate at the grain boundary. Quantitative contents at the grain boundary and inside the grain are presented in **Table 1**. In the reference sample (without PDT) the concentration of Na inside the grain is found to be around 15 ppm whereas the K concentration is below the detection limit. At the grain boundary, Na is the majority alkali with a Gibbsian interfacial excess (Γ) of 1.5 at nm^{-2}, compared to 0.5 at nm^{-2} for K. In the RbF-treated sample

© 2020 WILEY-VCH Verlag GmbH & Co. KGaA, Weinheim

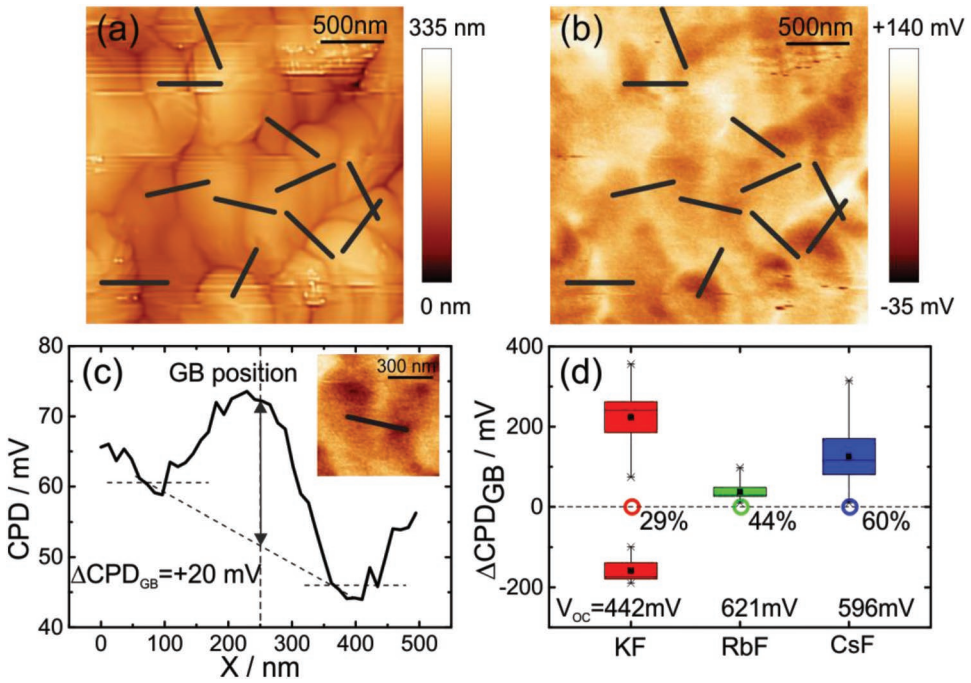

Figure 6. KPFM measurement of a RbF-treated Cu(In,Ga)Se_2 sample. a) Topography determined by AFM used to identify the positions of grain boundaries. b) Contact potential difference determined by KPFM, where the lines show where the potential profiles across grain boundaries were extracted. c) Contact potential difference across a single grain boundary with a positive potential variation. d) Statistical analysis of nearly 240 grain boundaries in Cu(In,Ga)Se_2 absorbers with KF-, RbF-, and CsF-PDT, indicating the average potential variation at grain boundaries. The relative amount of grain boundaries without any potential variation is indicated by the percentage numbers. The V_{OC} values from reference devices with a Zn(O,S) buffer layer are also stated. The KF-treated surface shows positive and negative band bending and the corresponding solar cell shows the lowest V_{OC}, whereas the RbF-treated surface shows the lowest and most homogeneous band bending at grain boundaries and the highest V_{OC}.

Rb and K are below the detection limit of APT inside the grain whereas Na significantly increases to 39 ppm. In another study, Rb has been found at a very low concentration also inside the grains by time-of-flight secondary ion mass spectroscopy.[77] At the grain boundary, even if all alkali elements are found to segregate, Rb is now the majority alkali at the grain boundary with $\Gamma = 1.6$ at nm^{-2}. Na and K show an equivalent segregation with $\Gamma = 0.4$ at nm^{-2}. Hence, the RbF-treated absorber demonstrates a clear segregation of Rb at the grain boundary, together with a decrease of the amount of Na and K. A significant increase of the Na content inside the grain interior is measured. Concerning absorber elements, in both cases, Cu depletion and In enrichment are observed at the grain boundary, the latter being slightly more pronounced when the RbF-PDT is applied. Accumulation of Rb at grain boundaries and dislocation cores has also been observed by TEM and X-ray fluorescence investigations of RbF-treated Cu(In,Ga)Se_2 absorbers and has been proposed as the cause of reduced bulk recombination.[78–80]

Thus, the observable bulk effects of heavy alkali PDT are: the nonradiative recombination is reduced, the amount of band tailing is reduced and the band bending, as well as the variation of band bending at grain boundaries is decreased along with the increase in open-circuit voltage. If band bending at the grain boundaries is reduced, the number of charged defects is reduced. This is likely caused by an accumulation of the heavy alkalis at the grain boundaries which can eliminate dangling bonds, Cu vacancies or other defects. These observations can explain an improvement of the open-circuit voltage. The alkali PDT leads to changes at the surface, but different electronic and chemical structures of the surface result in solar cells with the same improvement in open-circuit voltage. Whereas the differences observed in the bulk (different band bending at grain boundaries, different Urbach energies) do translate into differences of the observed open-circuit voltages. We therefore propose bulk effects, in particular changes at the grain boundaries, as the main driver for the increase of the open-circuit voltage.

If the main effect of the PDT with heavy alkalis is in the bulk and not at the surface, the question arises if the heavy alkalis could not be added before or during growth, instead of after the growth by a PDT. Several studies that compare the addition of heavy alkalis before or during growth with the PDT exist.[81–83] They all find that PDT is favorable, because the addition of heavy alkalis before or during growth leads to smaller grains,[81] a deep defect,[82] or increased inhomogeneity.[83] Thus, it appears that heavy alkalis during growth hinder the formation of large homogenous ordered crystals, and so it is necessary, to grow a high-quality film first and then modify the grain boundaries by an alkali-PDT to reduce their recombination activity.

The changes we discuss here due to the PDT with heavy alkalis (K, Rb, Cs) are always with respect to absorbers that contain Na. The positive effect of Na has long been known[13] and can be explained by the increased doping level due to the presence of Na,[15] where the Na can be added before or after the process. The PDT with heavy alkalis leads to modifications of the grain boundaries. The question arises why the heavy alkalis

© 2020 WILEY-VCH Verlag GmbH & Co. KGaA, Weinheim

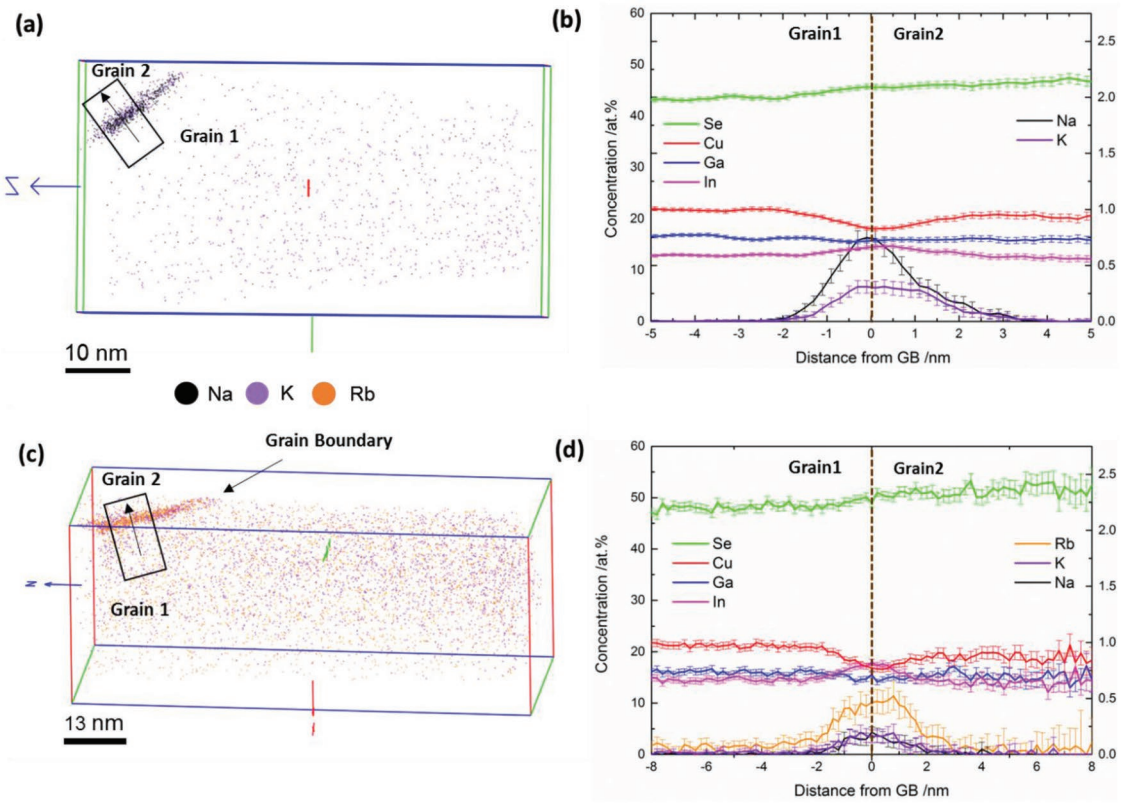

Figure 7. APT reconstruction at a grain boundary of a) an untreated high-temperature absorber and c) an absorber with RbF-PDT, showing $^{23}Na^+$ (black), $^{39}K^+$ (purple) and $^{85}Rb^+$ (orange) ions. b,d) Elemental profiles across the grain boundary of the respective samples. All alkalis segregate at the grain boundaries of the $Cu(In,Ga)Se_2$ absorber.

behave differently from Na at grain boundaries and inside the grains of $Cu(In,Ga)Se_2$.

3. Differences between Heavy and Light Alkalis

The differences between heavy and light alkalis can be traced back to the different phase diagrams of alkali-In-Se compounds and to the different effects of alkali impurities when diffusing in the $CuInSe_2$ or $Cu(In,Ga)Se_2$ matrix. **Figure 8**a shows migration energy barriers calculated for alkali impurities in $CuInSe_2$ within the vacancy migration mechanism.[42] An alkali atom moves from a substitutional Cu lattice site (x = 0.0) through a tetrahedral interstitial site (x = 0.5) to the neighboring Cu vacancy (x = 1.0). The barrier decreases from Li to K and then increases from K to Cs. The barriers are clearly wider for the light alkalis Li and Na than for those of the heavier alkali atoms. These features reflect the increase of the ionization potential or the tendency of bond formation toward Li and the increase of the ion size toward Cs. The right hand side of Figure 8a gives the formation energies for alkali atoms at substitutional Cu sites as bars extending over energies corresponding to the different stoichiometric conditions given by the chemical potentials of elements. The formation energy increases rapidly beyond Li and Na toward heavier alkali atoms, indicating low solubility of K, Rb, and Cs inside grains. Besides the vacancy mechanism, Li, Na, and K can also diffuse via interstitial mechanism in $CuInSe_2$, while the migration barrier is too high by this mechanism in the case of Rb and Cs.[42]

Alkalis interacting with $CuInSe_2$ may form a homogeneously alloyed single phase $Alk_xCu_{(1-x)}InSe_2$ or separate as an additional $AlkInSe_2$ phase. The calculated phase diagrams of the $Alk_xCu_{(1-x)}InSe_2$ systems are given in Figure 8b.[42] They are obtained by using the concept of the mixing parameter Ω for the mixing enthalpy $\Delta H_{mix} = x(1-x)\Omega$[84] and the mixing entropy $S = -k_B[x\ \ln(x) + (1-x)\ \ln(1-x)]$ of a random binary alloy. Fitting Ω at a dilute alkali impurity concentration of $x \approx 0.03$ to the calculated

Table 1. Gibbsian interfacial excess[35] values at the grain boundary and chemical composition for the alkali metals of untreated and RbF-treated samples at the grain boundary and within the grain measured with APT. The data taken at the RbF treated sample demonstrate Rb segregation at the grain boundary, accompanied by a reduction of Na and K. Na concentration in the grain is found to increase with RbF-PDT.

Sample	At grain boundary, Γ [at nm^{-2}]			Chemical composition in the grain [ppm]		
	Na	K	Rb	Na	K	Rb
No-PDT	1.2 ± 0.4	0.5 ± 0.2	–	15 ± 5	b.d.l[a)]	–
Rb-PDT	0.4 ± 0.1	0.4 ± 0.1	1.6 ± 0.4	39 ± 4	b.d.l	b.d.l

[a)]Below detection limit.

© 2020 WILEY-VCH Verlag GmbH & Co. KGaA, Weinheim

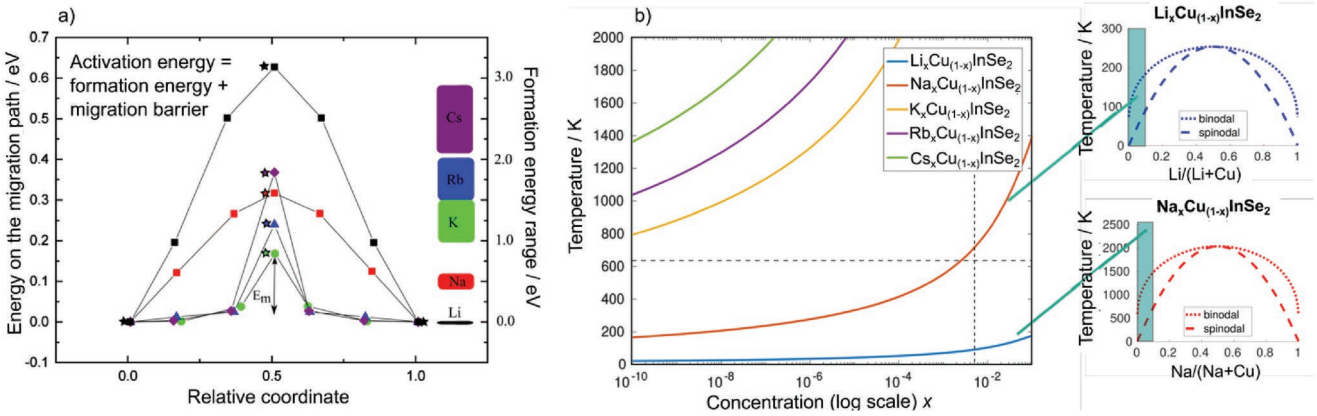

Figure 8. a) Theoretical migration barriers (markers connected with lines) for alkali metal impurities diffusing by the vacancy mechanism and Cu-site substitutional alkali impurity formation energies at different stoichiometric conditions (bars indicate the scatter of values, depending of the choice of chemical potentials). The activation energy (formation + migration energy) is much higher for the heavy alkalis: they are much less likely to form an Alk-on-Cu defect than Na or Li. b) Phase diagrams of the $Alk_xCu_{(1-x)}InSe_2$ compounds from hybrid functional DFT calculations. On the right hand side, the whole range $x = 0 \ldots 1$ is considered for Li and Na, whereas the left hand side gives results at low x values for all alkalis considered. The $Alk_xCu_{(1-x)}InSe_2$ phases are stable above the binodal curves (solid lines) whereas below them separation into the $AlkInSe_2$ and $CuInSe_2$ phases takes place. At treatment temperatures around 650 K only the light alkalis Li and Na can form a Cu-Alk-In selenide and be included in the bulk. The heavy alkalis K, Rb, and Cs will be in a two-phase state of separate $CuInSe_2$ and $AlkInSe_2$. Thus, in the case of heavy alkalis it is expected that an $AlkInSe_2$ phase will segregate at surfaces and interfaces but no alkali will be dissolved in the grains, whereas Na does not form a segregated phase at the surface but can be dissolved in the bulk of the grains.

enthalpy value, the Gibb's free energy is obtained for $x = 0 \ldots 1$ and the binodal (modulus) and spinodal curves discussed in ref. [85] are determined. They are shown on the right hand side of Figure 8b for Li and Na compounds. The binodal lines for all alkali compounds studied are shown on the left hand side of the figure for low alkali concentrations. Above the binodal curve the mixed phase $Alk_xCu_{(1-x)}InSe_2$ exists whereas below the curve the $AlkInSe_2$ and $CuInSe_2$ phases separate.[85] The horizontal and vertical dashed lines denote a typical PDT temperature of 350 °C and an alkali concentration of 0.1 at% for Na in the $Cu(In,Ga)Se_2$ absorber. Thus, according to the phase diagrams heavy alkalis are expected to form a separate Alk-In-Se compound. Indeed, secondary K-In-Se and Rb-In-Se phases have been found on some surfaces (K,[20,86] Rb[78,87]) but not on all (Rb[38,88]). The accumulation of heavy alkalis at grain boundaries indicates that structures similar to these additional phases also form there. We note that the observed alkali concentration of around 1 at nm^{-2} (Table 1) are not sufficient to claim the existence of an actual secondary phase. In contrast, the light alkalis Li and Na should form single phase Cu-Alk-In selenides and thus are more likely to dissolve into the grains, which is also in accordance with their low diffusion activation energies discussed above. This behavior is in line with the observation discussed above (Figure 7 and Table 1), that the heavy alkalis segregate more at the grain boundaries and push the lighter alkalis into the grain interior.

The separate Alk-In-Se compounds that have been found at surfaces after heavy alkali treatment support the trend of decreasing solubility with increasing atomic mass of the different alkali elements as well as the trend of the heavy alkalis to separate. This separation can explain the increased accumulation of heavy alkalis at grain boundaries where they can passivate dangling bonds and lower the density of fixed charges, thereby modifying the local band bending and the tail states.

4. Conclusion

An effect of KF-PDT on the surface has been found already in early studies after the introduction of KF-PDT, in particular the formation of a K-In-Se compound on low-temperature absorbers. Our investigations additionally confirm the accumulation of the heavy alkalis Rb and Cs at the surface of treated $Cu(In,Ga)Se_2$ absorbers. The surface bandgap of KF-treated absorbers is larger than that of untreated absorbers and agrees well with the calculated bandgap for $KInSe_2$, supporting the formation of this compound at the surface. However, this wider surface bandgap does not lead to a transport barrier in complete solar cell devices. Detailed XPS investigations show that the surfaces of treated high-temperature and low-temperature absorbers are quite different in terms of their chemical and electronic structure, in spite of the fact that all treatments lead to a similar improvement of the open-circuit voltage. Furthermore, no change in the surface morphology is observed in high-efficiency high-temperature absorbers upon treatment, whereas such change has been observed on high-efficiency low-temperature absorbers. Although the KF-, RbF-, or CsF-PDT can strongly modify the surface of the $Cu(In,Ga)Se_2$ absorber, it appears that this effect is not the main explanation for the improved open-circuit voltage. The open-circuit voltage improvement is rather due to an alkali-treatment-induced suppression of bulk recombination. This effect is achieved by a reduction in tail states and in the band bending at grain boundaries. We propose that the two effects are related, i.e., that the tail states are reduced because of the reduced band bending at the grain boundaries. There is a clear and characteristic accumulation of heavy alkalis at the grain boundaries, which can be explained by the tendency of heavy alkalis to form separate $AlkInSe_2$ compounds. The accumulation appears to be beneficial in reducing charged defects at

© 2020 WILEY-VCH Verlag GmbH & Co. KGaA, Weinheim

grain boundaries, thereby reducing the band bending and the resulting tail states.

5. Experimental Section

Absorber Preparation and PDT—High-Temperature Process: The high-temperature $Cu(In,Ga)Se_2$ solar cells were grown by ZSW on molybdenum coated alkali-aluminosilicate glass substrates by co-evaporation of Cu, In, Ga, and Se in a three-stage process. Subsequently, the $Cu(In,Ga)Se_2$ absorber was subjected to a KF-, RbF-, or CsF-PDT. Afterward, a CdS buffer was grown in a chemical bath. The highly resistive (Zn,Mg)O layer and the conductive Al-doped ZnO window layer were sputtered in vacuum. For complete solar cells the device structure was finished by depositing a Ni/Al/Ni grid. For the purpose of analysis the processing sequence was interrupted after $Cu(In,Ga)Se_2$ absorber or CdS buffer deposition.

Absorber Preparation and PDT—Low-Temperature Process: $Cu(In,Ga)Se_2$ thin films were prepared at Empa using co-evaporation of Cu, In, Ga, and Se from elemental sources at low substrate temperature (<450 °C) in high vacuum onto Mo-coated alkali-free substrates (flexible polyimide or soda-lime glass coated with SiO_x diffusion barrier). The multi-stage evaporation sequence was based on a modified three-stage process to obtain the desired indium to gallium grading across the thickness (see an example in ref. [33]). After the deposition, post-deposition treatments were applied in Se ambient using NaF followed by KF or RbF, at substrate temperatures ≈100 °C below those employed during the deposition of $Cu(In,Ga)Se_2$ films.

TEM: The $Cu(In,Ga)Se_2$ solar cell cross-section was prepared using a dual-beam focused ion beam-scanning electron microscope (FIB-SEM) by using the standard FIB lift-out method. The Zeiss NVision 40 FIB–SEM was operated with Ga ion beam.

The TEM lamella obtained was analyzed using a TEM, corrected for spherical aberration, ARM 200F from JEOL. Beam energy was lowered to 120 kV to reduce electron beam damage on the lamella. STEM mode combined with EDS was used to extract the elemental composition from the region of interest. The employed EDS silicon drift detector (SDD) is a windowless X-Max 100TLE from Oxford Instruments.

APT: APT samples in the form of conical shaped tips with an apex diameter less than 100 nm were prepared using FIB-SEM. The preparation of APT specimens parallel to the substrate is described elsewhere.[89] Laser assisted wide-angle tomographic atom probe (LAWATAP) was operated at 60 K under ultrahigh vacuum conditions (≈2×10^{-8} Pa). Field evaporation was triggered using femtosecond (10 nJ per pulse, 100 kHz) green ($\lambda = 515$ nm) laser pulses with a 100 µm laser beam diameter (full width half maximum). Data reconstructions in three dimensions were performed using the home built GPM 3Dsoft software.

PES: Lab-based photoemission spectroscopy measurements were conducted using non-monochromatized He I (21.2 eV, UPS) and Mg K_α (1253.56 eV, XPS) and a SPECS PHOIBOS 150 MCD-9 electron analyzer. The pass energy for XPS (UPS) was set to 30 eV (1 eV), resulting in a combined resolution for XPS (UPS) measurements of ≈1 eV (<100 meV).

Synchrotron-based hard X-ray photoelectron spectroscopy (HAXPES) experiments were conducted at the HiKE endstation[90] (2 keV) on the KMC-1 beamline[91] of the BESSY II electron storage ring, and at beamlines BL15XU[92] (6 keV) and BL47XU[93] (8 keV) of the SPring-8 electron storage ring. For all HAXPES spectra, the total energy resolution was ≈0.25 eV. For the 2 keV measurements, the samples were only briefly exposed to air (<5 min), while for the SPring-8 measurements the air exposure of the samples was significantly longer (a few hours). The excitation energy was calibrated by measuring multiple 4f spectra of a grounded, clean Au foil and setting the Au $4f_{7/2}$ binding energy equal to 84.00 eV.[94]

The relative composition of the samples was determined by fitting the XPS and HAXPES spectra of the respective shallow core levels with Voigt profiles and a linear background, and by taking the respective photoionization cross-sections into account.[51] Using different excitation energies will result in different kinetic energies and thus different IMFPs of the emitted photoelectrons,[48] allowing to derive a "depth-dependent" composition. A more detailed description can be found in ref. [24].

Device Simulation: At device level, the cell was simulated with the Sentaurus-TCAD suite, which solved the Poisson, electron and hole continuity, and the drift-diffusion carrier transport equations in coupled mode. Nonradiative recombination was described by the Shockley–Read–Hall (SRH) statistics. The solar cell was illuminated by the standard AM1.5G solar spectrum, and light propagation was modeled by the transfer matrix method (TMM). More details on the simulations and the parameter set we used can be found in ref. [47].

The simulated solar cell featured the standard stack made of Al-doped ZnO window and high resistive i-ZnO layer, CdS buffer, and $Cu(In,Ga)Se_2$ absorber with double-graded [Ga]/([Ga]+[In]) (GGI) composition of the type shown in ref. [4]. Both front and rear contacts were assumed to be ohmic, except for the simulations where a Schottky barrier was considered at the $Cu(In,Ga)Se_2$/Mo interface, as explicitly indicated.

DFT: The electronic and ionic structures of different bulk phases and the formation and migration energies of alkali metal impurities were calculated by the density functional theory as implemented in the VASP program package.[95] The impurity formation energies were calculated using supercells of 128 atoms and the formalism given, e.g., in ref. [96]. In particular, the results were corrected for finite supercell size errors in the electrostatic interactions using the method by Freysoldt et al.[97] For a reliable description of energy band positions and energy bandgaps the HSE06 hybrid functional was used.[98] The migration barriers of alkali impurities in $CuInSe_2$ were determined by using the climbing image nudged-elastic-band method (CI-NEB).[99] Due to the high computational cost, CI-NEB calculations were performed using a supercell of 64 atoms and the PBE exchange–correlation functional.[100] For further details, see refs. [42,101].

Current–Voltage and Admittance Characterization: Current–voltage measurements of completed solar cells were performed using a solar simulator at 25 °C in a 4-probe configuration.

For temperature dependent IV measurements (IVT), solar cells were mounted in an evacuated closed-cycle cryostat in the dark. Sample temperature was measured with a Si diode sensor glued onto an identical glass substrate next to the solar cell. IVT characteristics were recorded in steps of 10 K after temperature stabilization while cooling down from 320–20 K set temperature (≈320–45 K measured temperature). Dark and illuminated IV curves were measured at each temperature with a shutter and neutral density filter wheel assembly. After IVT measurements, the sample was heated to 300 K and kept in the dark overnight for at least 12 h. The admittance spectrum was recorded with an inductance (L), capacitance (C), resistance (R) meter (frequency: 100 Hz–1 MHz, ac voltage amplitude: 30 mV rms) in the same temperature range while cooling down again from 320–20 K set temperature.

Photoluminescence: Photoluminescence was measured in a home-built system, as described in ref. [102]. The samples were excited by the 660 nm wavelength light of a laser diode. The samples were either in air for room temperature measurements or in a He-flow cryostat for low temperature measurements. The detection set-up was calibrated by the known spectrum of a calibrated halogen lamp.

Radiative efficiency and quasi-Fermi level splitting were determined as described in ref. [103].

Urbach energies were extracted from absorption spectra determined from the photoluminescence spectra, according to the (1-R) method discussed in ref. [62].

Quantum Efficiency: Measurements of the external quantum efficiency were performed using chopped (260 Hz) monochromatic light with the cell at a temperature of 25 °C and at 0 V bias voltage, using a certified Si cell as reference. A bias illumination with an intensity of ≈100 W m^{-2} was additionally applied.

Photocurrent Spectroscopy: For photocurrent spectroscopy measurements, full $Cu(In,Ga)Se_2$ solar cells in short circuit were illuminated using a combination of mechanically chopped monochromatic light—used to determine the wavelength dependence

© 2020 WILEY-VCH Verlag GmbH & Co. KGaA, Weinheim

of the photocurrent—and continuous white bias illumination. The white light intensity was adjusted to induce a dc current at least two orders of magnitude higher than the photocurrent resulting from the monochromatic illumination—enabling to keep constant the product between the mobility and lifetime of charge carriers (dual-beam photocurrent spectroscopy method). In these conditions, the detected photocurrent can be considered as proportional to the fraction of the coefficient of absorption related to electrically active defects. The photocurrent was amplified using a low noise current-to-voltage preamplifier, measured using a lock-in amplifier referenced to the monochromatic light pulsing frequency and normalized to the flux of incident photons. The Urbach parameter was determined by fitting the exponential decay observed on normalized photocurrent spectra below the optical bandgap (fitting in an energy range of 0.05 eV).

KPFM: KPFM measurements were carried out using a scanning probe microscope (Omicron Nanotechnology GmbH), controlled by a Nanonis controller (SPECS Zurich GmbH). Pt/Ir-coated Si cantilevers (Nanosensors) were used (f_0 ≈165 kHz). Amplitude modulation (AM) KPFM[104] at the second resonance frequency of the cantilever (f_2 ≈1.035 MHz) was used for the detection of the CPD, where CPD = $\Phi_{sample} - \Phi_{tip}$. The work function of the tip (Φ_{tip}) was calibrated using an Au reference sample.

Supporting Information

Supporting Information is available from the Wiley Online Library or from the author.

Acknowledgements

This work was supported by the European Union's Horizon 2020 research and innovation program under grant agreement no. 641004 (Sharc25) and by the Swiss State Secretariat for Education, Research and Innovation (SERI) under contract number 15.0158.

Conflict of Interest

The authors declare no conflict of interest.

Keywords

alkali treatment, bulk, chalcopyrite solar cells, grain boundaries, recombination, surface

Received: November 14, 2019
Revised: December 12, 2019
Published online:

[1] UNEP, in *Green Energy Choices: The Benefits, Risks and Trade-offs of Low-Carbon Technologies for Electricity Production* (Eds: E. G. Hertwich, J. Aloisi de Larderel, A. Arvesen, P. Bayer, J. Bergesen, E. Bouman, T. Gibon, G. Heath, C. Peña, P. Purohit, A. Ramirez, S. Suh), Report of the International Resource Panel, **2016**.
[2] A. Chirila, P. Reinhard, F. Pianezzi, P. Bloesch, A. R. Uhl, C. Fella, L. Kranz, D. Keller, C. Gretener, H. Hagendorfer, D. Jaeger, R. Erni, S. Nishiwaki, S. Buecheler, A. N. Tiwari, *Nat. Mater.* **2013**, *12*, 1107.
[3] P. Jackson, D. Hariskos, R. Wuerz, W. Wischmann, M. Powalla, *Phys. Status Solidi RRL* **2014**, *8*, 219.
[4] P. Jackson, D. Hariskos, R. Wuerz, O. Kiowski, A. Bauer, T. M. Friedlmeier, M. Powalla, *Phys. Status Solidi RRL* **2015**, *9*, 28.
[5] P. Jackson, R. Wuerz, D. Hariskos, E. Lotter, W. Witte, M. Powalla, *Phys. Status Solidi RRL* **2016**, *10*, 583.
[6] a) Solar Frontier, Solar Frontier Achieves World Record Thin-Film Solar Cell Efficiency of 23.35%, http://www.solar-frontier.com/eng/news/2019/0117_press.html (accessed: January 2019); b) M. Nakamura, K. Yamaguchi, Y. Kimoto, Y. Yasaki, T. Kato, H. Sugimoto, *46th IEEE Photovoltaic Specialist Conf.*, IEEE, Chicago **2019**.
[7] T. Kato, *Jpn. J. Appl. Phys.* **2017**, *56*, 04CA02.
[8] M. Edoff, T. Jarmar, N. S. Nilsson, E. Wallin, D. Hogstrom, O. Stolt, O. Lundberg, W. Shafarman, L. Stolt, *IEEE J. Photovoltaics* **2017**, *7*, 1789.
[9] L. M. Mansfield, R. Noufi, C. P. Muzzillo, C. DeHart, K. Bowers, B. To, J. W. Pankow, R. C. Reedy, K. Ramanathan, *IEEE J. Photovoltaics* **2014**, *4*, 1650.
[10] T. Feurer, F. Fu, T. P. Weiss, E. Avancini, J. Löckinger, S. Buecheler, A. N. Tiwari, *Thin Solid Films* **2019**, *670*, 34.
[11] S. Zahedi-Azad, M. Maiberg, R. Clausing, R. Scheer, *Thin Solid Films* **2019**, *669*, 629.
[12] O. Lundberg, E. Wallin, V. Gusak, S. Södergren, S. Chen, S. Lotfi, F. Chalvet, U. Malm, N. Kaihovirta, P. Mende, G. Jaschke, P. Kratzert, J. Joel, M. Skupinski, P. Lindberg, T. Jarmar, J. Lundberg, J. Mathiasson, L. Stolt, *43rd Photovoltaic Specialist Conf.*, IEEE, Denver **2016**, p. 1293.
[13] J. Hedström, H. Ohlsén, M. Bodegard, A. Kylner, L. Stolt, D. Hariskos, M. Ruckh, H.-W. Schock, *23rd IEEE Photovoltaic Specialist Conf.*, IEEE, Piscataway, NJ **1993**.
[14] D. Abou-Ras, S. Wagner, B. J. Stanbery, H.-W. Schock, R. Scheer, L. Stolt, S. Siebentritt, D. Lincot, C. Eberspacher, K. Kushiya, A. N. Tiwari, *Thin Solid Films* **2017**, *633*, 2.
[15] D. Rudmann, D. Brémaud, H. Zogg, A. N. Tiwari, *J. Appl. Phys.* **2005**, *97*, 084903.
[16] A. Rockett, *Thin Solid Films* **2005**, *480–481*, 2.
[17] F. Pianezzi, P. Reinhard, A. Chirila, B. Bissig, S. Nishiwaki, S. Buecheler, A. N. Tiwari, *Phys. Chem. Chem. Phys.* **2014**, *16*, 8843.
[18] A. Laemmle, R. Wuerz, M. Powalla, *Phys. Status Solidi RRL* **2013**, *7*, 631.
[19] P. Pistor, D. Greiner, C. A. Kaufmann, S. Brunken, M. Gorgoi, A. Steigert, W. Calvet, I. Lauermann, R. Klenk, T. Unold, M.-C. Lux-Steiner, *Appl. Phys. Lett.* **2014**, *105*, 063901.
[20] E. Handick, P. Reinhard, J.-H. Alsmeier, L. Köhler, F. Pianezzi, S. Krause, M. Gorgoi, E. Ikenaga, N. Koch, R. G. Wilks, S. Buecheler, A. N. Tiwari, M. Bär, *ACS Appl. Mater. Interfaces* **2015**, *7*, 27414.
[21] P. Reinhard, B. Bissig, F. Pianezzi, E. Avancini, H. Hagendorfer, D. Keller, P. Fuchs, M. Döbeli, C. Vigo, P. Crivelli, S. Nishiwaki, S. Buecheler, A. N. Tiwari, *Chem. Mater.* **2015**, *27*, 5755.
[22] T. Lepetit, S. Harel, L. Arzel, G. Ouvrard, N. Barreau, *IEEE J. Photovoltaics* **2016**, *6*, 1316.
[23] C. P. Muzzillo, L. M. Mansfield, K. Ramanathan, T. J. Anderson, *J. Mater. Sci.* **2016**, *51*, 6812.
[24] E. Handick, P. Reinhard, R. G. Wilks, F. Pianezzi, T. Kunze, D. Kreikemeyer-Lorenzo, L. Weinhardt, M. Blum, W. Yang, M. Gorgoi, E. Ikenaga, D. Gerlach, S. Ueda, Y. Yamashita, T. Chikyow, C. Heske, S. Buecheler, A. N. Tiwari, M. Bär, *ACS Appl. Mater. Interfaces* **2017**, *9*, 3581.
[25] B. Umsur, W. Calvet, A. Steigert, I. Lauermann, M. Gorgoi, K. Prietzel, D. Greiner, C. A. Kaufmann, T. Unold, M. C. Lux-Steiner, *Phys. Chem. Chem. Phys.* **2016**, *18*, 14129.
[26] C. P. Muzzillo, *Sol. Energy Mater. Sol. Cells* **2017**, *172*, 18.

© 2020 WILEY-VCH Verlag GmbH & Co. KGaA, Weinheim

[27] R. Scheer, H. W. Schock, *Chalcogenide Photovoltaics: Physics, Technologies, and Thin Film Devices*, Wiley-VCH, Weinheim **2011**.
[28] I. Khatri, H. Fukai, H. Yamaguchi, M. Sugiyama, T. Nakada, *Sol. Energy Mater. Sol. Cells* **2016**, *155*, 280.
[29] a) I. Khatri, J. Matsuura, M. Sugiyama, T. Nakada, *Prog. Photovoltaics* **2019**, *27*, 22; b) T. Lepetit, *Vol. Doctoral Thesis*, Nantes **2015**; c) S. A. Jensen, S. Glynn, A. Kanevce, P. Dippo, J. V. Li, D. H. Levi, D. Kuciauskas, *J. Appl. Phys.* **2016**, *120*, 063106.
[30] a) A. Laemmle, R. Wuerz, T. Schwarz, O. Cojocaru-Mirédin, P.-P. Choi, M. Powalla, *J. Appl. Phys.* **2014**, *115*, 154501; b) D. Abou-Ras, S. S. Schmidt, R. Caballero, T. Unold, H. W. Schock, C. T. Koch, B. Schaffer, M. Schaffer, P. P. Choi, O. Cojocaru-Miredin, *Adv. Energy Mater.* **2012**, *2*, 992.
[31] O. Cojocaru-Miredin, C. Pyuck-Pa, D. Abou-Ras, S. S. Schmidt, R. Caballero, D. Raabe, *IEEE J. Photovoltaics* **2011**, *1*, 207.
[32] D. Shin, J. Kim, T. Gershon, R. Mankad, M. Hopstaken, S. Guha, B. T. Ahn, B. Shin, *Sol. Energy Mater. Sol. Cells* **2016**, *157*, 695.
[33] A. Chirila, S. Buecheler, F. Pianezzi, P. Bloesch, C. Gretener, A. R. Uhl, C. Fella, L. Kranz, J. Perrenoud, S. Seyrling, R. Verma, S. Nishiwaki, Y. E. Romanyuk, G. Bilger, A. N. Tiwari, *Nat. Mater.* **2011**, *10*, 857.
[34] R. Carron, S. Nishiwaki, T. Feurer, R. Hertwig, E. Avancini, J. Löckinger, S.-C. Yang, S. Buecheler, A. N. Tiwari, *Adv. Energy Mater.* **2019**, *9*, 1900408.
[35] A. Vilalta-Clemente, M. Raghuwanshi, S. Duguay, C. Castro, E. Cadel, P. Pareige, P. Jackson, R. Wuerz, D. Hariskos, W. Witte, *Appl. Phys. Lett.* **2018**, *112*, 103105.
[36] M. Raghuwanshi, A. Vilalta-Clemente, C. Castro, S. Duguay, E. Cadel, P. Jackson, D. Hariskos, W. Witte, P. Pareige, *Nano Energy* **2019**, *60*, 103.
[37] P. Reinhard, B. Bissig, F. Pianezzi, H. Hagendorfer, G. Sozzi, R. Menozzi, C. Gretener, S. Nishiwaki, S. Buecheler, A. N. Tiwari, *Nano Lett.* **2015**, *15*, 3334.
[38] D. Kreikemeyer-Lorenzo, D. Hauschild, P. Jackson, T. M. Friedlmeier, D. Hariskos, M. Blum, W. L. Yang, F. Reinert, M. Powalla, C. Heske, L. Weinhardt, *ACS Appl. Mater. Interfaces* **2018**, *10*, 37602.
[39] N. Taguchi, S. Tanaka, S. Ishizuka, *Appl. Phys. Lett.* **2018**, *113*, 113903.
[40] W. Gong, M. A. Faist, N. J. Ekins-Daukes, Z. Xu, D. D. C. Bradley, J. Nelson, T. Kirchartz, *Phys. Rev. B* **2012**, *86*, 024201.
[41] T. Kodalle, R. Kormath Madam Raghupathy, T. Bertram, N. Maticiuc, H. A. Yetkin, R. Gunder, R. Schlatmann, T. D. Kühne, C. A. Kaufmann, H. Mirhosseini, *Phys. Status Solidi RRL* **2019**, *13*, 1800564.
[42] M. Malitckaya, H. P. Komsa, V. Havu, M. J. Puska, *J. Phys. Chem. C* **2017**, *121*, 15516.
[43] T. P. Weiss, S. Nishiwaki, B. Bissig, R. Carron, E. Avancini, J. Lockinger, S. Buecheler, A. N. Tiwari, *Adv. Mater. Interfaces* **2018**, *5*, 1701007.
[44] M. Malitckaya, *Vol. Doctoral Thesis*, Aalto University, Helsinki **2019**.
[45] E. Ghorbani, P. Erhart, K. Albe, *Phys. Rev. Mater.* **2019**, *3*, 075401.
[46] F. Werner, M. H. Wolter, S. Siebentritt, G. Sozzi, S. D. Napoli, R. Menozzi, P. Jackson, W. Witte, R. Carron, E. Avancini, T. Weiss, S. Buecheler, *Prog. Photovoltaics* **2018**, *26*, 911.
[47] G. Sozzi, S. D. Napoli, R. Menozzi, F. Werner, S. Siebentritt, P. Jackson, W. Witte, *44th Photovoltaic Specialist Conf. (PVSC)*, IEEE, Piscataway, NJ **2017**.
[48] S. Tanuma, C. J. Powell, D. R. Penn, *Surf. Interface Anal.* **1994**, *21*, 165.
[49] E. Handick, P. Reinhard, R. G. Wilks, F. Pianezzi, R. Félix, M. Gorgoi, T. Kunze, S. Buecheler, A. N. Tiwari, M. Bär, *43rd Photovoltaic Specialists Conference (PVSC)*, IEEE, Piscataway, NJ **2016**.
[50] Please note that for the data points representing the most surface sensitive measurements (i.e., K:Se ratio determined from Mg K_α data [$h\nu = 1253.56$ eV] and VBM measured with He I [$h\nu = 21.2$ eV]), the inelastic mean free paths of the involved photoelectrons differs (3 nm [Mg K_α] and < 1 nm [He I]). Therefore, in this case the VBM relates to a region closer to the CIGSe surface than the respective K:Se value, which could increase the uncertainty in case of a pronounced structure gradient very near the surface.
[51] a) M. B. Trzhaskovskaya, V. K. Nikulin, V. I. Nefedov, V. G. Yarzhemsky, *At. Data Nucl. Data Tables* **2006**, *92*, 245; b) M. B. Trzhaskovskaya, V. I. Nefedov, V. G. Yarzhemsky, *At. Data Nucl. Data Tables* **2001**, *77*, 97.
[52] D. Hauschild, D. Kreikemeyer-Lorenzo, P. Jackson, T. M. Friedlmeier, D. Hariskos, F. Reinert, M. Powalla, C. Heske, L. Weinhardt, *ACS Energy Lett.* **2017**, *2*, 2383.
[53] E. Avancini, R. Carron, T. P. Weiss, C. Andres, M. Bürki, C. Schreiner, R. Figi, Y. E. Romanyuk, S. Buecheler, A. N. Tiwari, *Chem. Mater.* **2017**, *29*, 9695.
[54] F. Babbe, H. Elanzeery, M. Melchiorre, A. Zelenina, S. Siebentritt, *Phys. Rev. Mater.* **2018**, *2*, 105405.
[55] D. Regesch, L. Gütay, J. K. Larsen, V. Deprédurand, D. Tanaka, Y. Aida, S. Siebentritt, *Appl. Phys. Lett.* **2012**, *101*, 112108.
[56] M. H. Wolter, B. Bissig, E. Avancini, R. Carron, S. Buecheler, P. Jackson, S. Siebentritt, *IEEE J. Photovoltaics* **2018**, *8*, 1320.
[57] a) W. Shockley, H. J. Queisser, *J. Appl. Phys.* **1961**, *32*, 510; b) P. Würfel, *J. Phys. C: Solid State Phys.* **1982**, *15*, 3967.
[58] F. Babbe, L. Choubrac, S. Siebentritt, *Sol. RRL* **2018**, *2*, 1800248.
[59] S. De Wolf, J. Holovsky, S.-J. Moon, P. Löper, B. Niesen, M. Ledinsky, F.-J. Haug, J.-H. Yum, C. Ballif, *J. Phys. Chem. Lett.* **2014**, *5*, 1035.
[60] S. Siebentritt, G. Rey, A. Finger, J. Sendler, T. P. Weiss, D. Regesch, T. Bertram, *Sol. Energy Mater. Sol. Cells* **2016**, *158*, 126.
[61] F. Urbach, *Phys. Rev.* **1953**, *92*, 1324.
[62] G. Rey, C. Spindler, S. Siebentritt, M. Nuys, R. Carius, S. Li, C. Platzer-Björkman, *Phys. Rev. Appl.* **2018**, *9*, 064008.
[63] M. D. Sturge, *Phys. Rev.* **1962**, *127*, 768.
[64] M. A. Green, Y. Hishikawa, E. D. Dunlop, D. H. Levi, J. Hohl-Ebinger, A. W. Y. Ho-Baillie, *Prog. Photovoltaics* **2018**, *26*, 427.
[65] G. D. Cody, *J. Non-Cryst. Solids* **1992**, *141*, 3.
[66] R. Carron, E. Avancini, T. Feurer, B. Bissig, P. A. Losio, R. Figi, C. Schreiner, M. Bürki, E. Bourgeois, Z. Remes, M. Nesladek, S. Buecheler, A. N. Tiwari, *Sci. Technol. Adv. Mater.* **2018**, *19*, 396.
[67] a) I. Dirnstorfer, M. Wagner, D. M. Hofmann, M. D. Lampert, F. Karg, B. K. Meyer, *Phys. Status Solidi A* **1998**, *168*, 163; b) A. Bauknecht, S. Siebentritt, J. Albert, M. C. Lux-Steiner, *J. Appl. Phys.* **2001**, *89*, 4391.
[68] C. S. Schnohr, S. Eckner, P. Schöppe, E. Haubold, F. d'Acapito, D. Greiner, C. A. Kaufmann, *Acta Mater.* **2018**, *153*, 8.
[69] J. Mattheis, U. Rau, J. Werner, *J. Appl. Phys.* **2007**, *101*, 113519.
[70] U. Rau, K. Taretto, S. Siebentritt, *Appl. Phys. A* **2009**, *96*, 221.
[71] N. Nicoara, R. Manaligod, P. Jackson, D. Hariskos, W. Witte, G. Sozzi, R. Menozzi, S. Sadewasser, *Nat. Commun.* **2019**, *10*, 3980.
[72] R. Baier, C. Leendertz, D. Abou-Ras, M. C. Lux-Steiner, S. Sadewasser, *Sol. Energy Mater. Sol. Cells* **2014**, *130*, 124.
[73] S. Sadewasser, T. Glatzel, S. Schuler, S. Nishiwaki, R. Kaigawa, M. C. Lux-Steiner, *Thin Solid Films* **2003**, *431–432*, 257.
[74] N. Nicoara, T. Lepetit, L. Arzel, S. Harel, N. Barreau, S. Sadewasser, *Sci. Rep.* **2017**, *7*, 41361.
[75] K. Taretto, U. Rau, *J. Appl. Phys.* **2008**, *103*, 094523.
[76] a) K. Taretto, U. Rau, J. Werner, *Thin Solid Films* **2005**, *480–481*, 8; b) M. Gloeckler, J. R. Sites, W. K. Metzger, *J. Appl. Phys.* **2005**, *98*, 113704.

© 2020 WILEY-VCH Verlag GmbH & Co. KGaA, Weinheim

[77] R. Wuerz, W. Hempel, P. Jackson, *J. Appl. Phys.* **2018**, *124*, 165305.
[78] T. Kodalle, M. D. Heinemann, D. Greiner, H. A. Yetkin, M. Klupsch, C. Li, P. A. van Aken, I. Lauermann, R. Schlatmann, C. A. Kaufmann, *Sol. RRL* **2018**, *2*, 1800156.
[79] P. Schöppe, S. Schönherr, R. Wuerz, W. Wisniewski, G. Martínez-Criado, M. Ritzer, K. Ritter, C. Ronning, C. S. Schnohr, *Nano Energy* **2017**, *42*, 307.
[80] P. Schöppe, S. Schönherr, P. Jackson, R. Wuerz, W. Wisniewski, M. Ritzer, M. Zapf, A. Johannes, C. S. Schnohr, C. Ronning, *ACS Appl. Mater. Interfaces* **2018**, *10*, 40592.
[81] A. Laemmle, R. Wuerz, M. Powalla, *Thin Solid Films* **2015**, *582*, 27.
[82] F. Pianezzi, P. Reinhard, A. Chirilă, S. Nishiwaki, B. Bissig, S. Buecheler, A. N. Tiwari, *J. Appl. Phys.* **2013**, *114*, 194508.
[83] O. Donzel-Gargand, T. Thersleff, J. Keller, T. Torndahl, F. Larsson, E. Wallin, L. Stolt, M. Edoff, *Prog. Photovoltaics* **2018**, *26*, 730.
[84] S.-H. Wei, S. B. Zhang, A. Zunger, *J. Appl. Phys.* **1999**, *85*, 7214.
[85] D. Hariskos, M. Powalla, *J. Mater. Res.* **2017**, *32*, 3789.
[86] M. Malitckaya, T. Kunze, H.-P. Komsa, V. Havu, E. Handick, R. G. Wilks, M. Bär, M. J. Puska, *ACS Appl. Mater. Interfaces* **2019**, *11*, 3024.
[87] a) S. Ishizuka, N. Taguchi, J. Nishinaga, Y. Kamikawa, S. Tanaka, H. Shibata, *J. Phys. Chem. C* **2018**, *122*, 3809; b) N. Maticiuc, T. Kodalle, J. Lauche, R. Wenisch, T. Bertram, C. A. Kaufmann, I. Lauermann, *Thin Solid Films* **2018**, *665*, 143.
[88] N. Nicoara, T. Kunze, P. Jackson, D. Hariskos, R. F. Duarte, R. G. Wilks, W. Witte, M. Bär, S. Sadewasser, *ACS Appl. Mater. Interfaces* **2017**, *9*, 44173.
[89] M. Raghuwanshi, *Vol. Doctoral Thesis*, University of Rouen **2016**.
[90] M. Gorgoi, S. Svensson, F. Schafers, G. Öhrwall, M. Mertin, P. Bressler, O. Karis, H. Siegbahn, A. Sandell, H. Rensmo, W. Doherty, C. Jung, W. Braun, W. Eberhardt, *Nucl. Instrum. Methods Phys. Res., Sect. A* **2009**, *601*, 48.
[91] F. Schaefers, M. Mertin, M. Gorgoi, *Rev. Sci. Instrum.* **2007**, *78*, 123102.
[92] a) S. Ueda, *J. Electron Spectrosc. Relat. Phenom.* **2013**, *190*, 235; b) S. Ueda, Y. Katsuya, M. Tanaka, H. Yoshikawa, Y. Yamashita, S. Ishimaru, Y. Matsushita, K. Kobayashi, *AIP Conf. Proc.* **2010**, *1234*, 403.
[93] E. Ikenaga, M. Kobata, H. Matsuda, T. Sugiyama, H. Daimon, K. Kobayashi, *J. Electron Spectrosc. Relat. Phenom.* **2013**, *190*, 180.
[94] M. P. Seah, I. S. Gilmore, G. Beamson, *Surf. Interface Anal.* **1998**, *26*, 642.
[95] a) G. Kresse, J. Furthmuller, *Phys. Rev. B* **1996**, *54*, 11169; b) G. Kresse, J. Furthmuller, *Comput. Mater. Sci.* **1996**, *6*, 15.
[96] C. Freysoldt, B. Grabowski, T. Hickel, J. Neugebauer, G. Kresse, A. Janotti, C. G. Van de Walle, *Rev. Mod. Phys.* **2014**, *86*, 253.
[97] C. Freysoldt, J. Neugebauer, C. G. Van de Walle, *Phys. Status Solidi B* **2011**, *248*, 1067.
[98] a) J. Heyd, G. E. Scuseria, M. Ernzerhof, *J. Chem. Phys.* **2006**, *124*, 219906; b) J. Heyd, G. E. Scuseria, M. Ernzerhof, *J. Chem. Phys.* **2003**, *118*, 8207.
[99] G. Henkelman, H. Jonsson, *J. Chem. Phys.* **2000**, *113*, 9978.
[100] a) J. P. Perdew, K. Burke, M. Ernzerhof, *Phys. Rev. Lett.* **1997**, *78*, 1396; b) J. P. Perdew, K. Burke, M. Ernzerhof, *Phys. Rev. Lett.* **1996**, *77*, 3865.
[101] M. Malitckaya, H.-P. Komsa, V. Havu, M. J. Puska, *Adv. Electron. Mater.* **2017**, *3*, 1600353.
[102] C. Spindler, D. Regesch, S. Siebentritt, *Appl. Phys. Lett.* **2016**, *109*, 032105.
[103] a) L. Gütay, G. H. Bauer, *Thin Solid Films* **2007**, *515*, 6212; b) F. Babbe, L. Choubrac, S. Siebentritt, *Appl. Phys. Lett.* **2016**, *109*, 082105.
[104] T. Glatzel, S. Sadewasser, M. C. Lux-Steiner, *Appl. Surf. Sci.* **2003**, *210*, 84.

© 2020 WILEY-VCH Verlag GmbH & Co. KGaA, Weinheim